# Symmetry-breaking 60°-spin order in the *A*-site-ordered perovskite $LaMn_3V_4O_{12}$

Takashi Saito (齊藤高志),[1,*] Masayuki Toyoda (豊田雅之),[2,3] Clemens Ritter,[4] Shoubao Zhang (张守宝),[1] Tamio Oguchi (小口多美夫),[2,3] J. Paul Attfield,[5] and Yuichi Shimakawa (島川祐一)[1,3]

[1]*Institute for Chemical Research, Kyoto University, Uji, Kyoto 611-0011, Japan*

[2]*Institute of Scientific and Industrial Research, Osaka University, 8-1, Mihogaoka, Ibaraki, Osaka 567-0047, Japan*

[3]*Japan Science and Technology Agency, CREST, Gobancho, Chiyoda-ku, Tokyo, 102-0076, Japan*

[4]*Institut Laue-Langevin, BP 156, F-38042, Grenoble Cedex 9, France*

[5]*Centre for Science at Extreme Conditions and School of Chemistry, University of Edinburgh, Mayfield Road, Edinburgh EH9 3JZ, United Kingdom*

(Received 1 August 2014; revised manuscript received 27 October 2014; published 1 December 2014)

The magnetism of the *A*-site-ordered perovskite $LaMn_3V_4O_{12}$ is studied comprehensively by means of neutron powder diffraction experiments and theoretical calculations. Magnetic neutron diffraction results show that a rhombohedral 60° spin structure emerges on the cubic lattice below a 44-K Néel transition. *Ab initio* electronic structure calculations confirm that high-spin $Mn^{2+}$ moments are localized while V 3*d*-band states are itinerant, and that the noncollinear 60° spin structure is more stable than collinear ferromagnetic or G-type antiferromagnetic alternatives. Effective Heisenberg model calculations reveal that the appearance of such a nontrivial spin structure can be attributed to significant next-nearest-neighbor and third-nearest-neighbor magnetic interactions.

DOI: 10.1103/PhysRevB.90.214405 PACS number(s): 75.25.−j, 61.05.F−, 71.20.−b, 75.30.Et

## I. INTRODUCTION

Competing magnetic interactions in solids often stabilize noncollinear spin structures with adjacent spins at intermediate angles between parallel and antiparallel arrangements [1]. For example, antiferromagnetic interactions in a triangular Heisenberg lattice produce geometric spin frustration, resulting in a 120° spin structure at the ground state [2]. Competition between the ferromagnetic (FM) nearest-neighbor (NN) interactions and antiferromagnetic (AFM) next-nearest-neighbor (NNN) interactions in orthorhombic perovskite $TbMnO_3$ produces a spiral spin ordering [3]. The noncollinear spin structure in $TbMnO_3$ induces ferroelectric structural distortions through Dzyaloshinsky-Moriya interaction [4,5], and the compound is multiferroic, with both ferromagnetic and ferroelectric properties [6–10]. Nontrivial spin structures are therefore attractive as a platform for exploring novel functional properties.

Perovskite-structured transition-metal oxides have a large variety of magnetic structures. Although the ideal perovskite structure $ABO_3$ is cubic, most of these oxides are distorted with tilted octahedra, making the network of magnetic interactions in these compounds more complicated. Screw-type spin ordering due to competing AFM- and FM-NN interactions in cubic $SrFeO_3$ is a rare example [11–14]. We recently found that the *A*-site magnetism in the *A*-site-ordered perovskite-structure compounds $CaCu_3B_4O_{12}$ ($B$ = nonmagnetic Sn, Ti, and Ge) provide an excellent model system that has an $S = 1/2$ cubic spin lattice, where either ferromagnetism or antiferromagnetism can be stabilized [15–18]. Here we focus on the spin structure of $LaMn_3V_4O_{12}$, which crystallizes in an *A*-site-ordered perovskite structure having cubic $Im\bar{3}$ symmetry, with Mn occupying 3/4 of the *A* sites (inset of Fig. 1) [19]. The $VO_6$ octahedra are heavily tilted, forming a square-planar oxygen coordination at the Mn site. Bond valence sum calculations and x-ray absorption spectroscopy of $LaMn_3V_4O_{12}$ have shown that the Mn is divalent and the V has a +3/+4 mixed-valence state.

In this study, we found a noncollinear 60° spin structure in the spin lattice of $LaMn_3V_4O_{12}$. The nontrivial symmetry-breaking spin structure on a cubic crystal lattice has been revealed by neutron powder diffraction, and the stability of the magnetic ground state was evaluated by using first-principles theoretical calculations and effective Heisenberg model calculations.

## II. EXPERIMENTAL METHODS

A polycrystalline sample of $LaMn_3V_4O_{12}$ was prepared under a high-pressure and high-temperature condition using a cubic anvil press, as reported previously [19]. Magnetic susceptibility was measured using a superconducting quantum interference device (SQUID) magnetometer (MPMS, Quantum Design) in an external field of 1 T. Neutron powder diffraction experiments with a wavelength of 1.59 Å were performed at the D2B diffractometer (ILL, France) at 2 and 300 K. Rietveld refinements of the diffraction patterns were performed with the FULLPROF [20] program, and magnetic symmetry analysis was done using the BASIREPS program [21,22].

The Vienna *ab initio* simulation package (VASP) [23–26] was used to evaluate the electronic structure of $LaMn_3V_4O_{12}$ by first-principles density-functional theory (DFT) calculations within the generalized gradient approximation (GGA) [27,28] in combination with projector augmented wave potentials [29,30]. Experimentally obtained crystal structure parameters at 2 K were used in the calculations. The spin-orbit coupling term was included. The valence wave functions were expanded in a plane wave basis up to a cutoff energy of 500 eV. A $6 \times 6 \times 6$ $k$-point grid was used for the Brillouin zone integration. The strong correlation effect of Mn-3*d* electrons was described by adding the effective on-site Coulomb interaction $U_{\text{eff}} = 5$ eV according to the formulation

*Corresponding author: saito@scl.kyoto-u.ac.jp

 

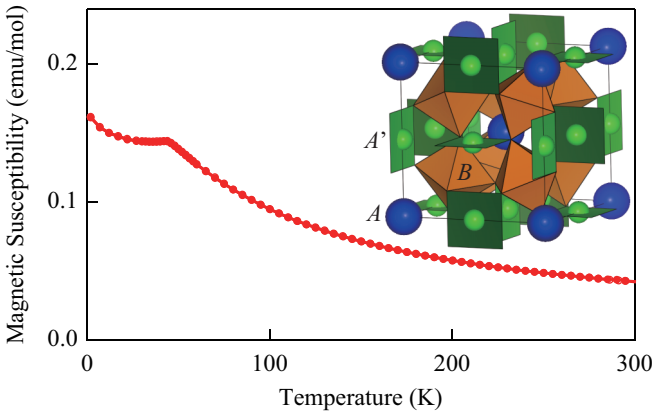


FIG. 1. (Color online) Temperature dependence of the magnetic susceptibility of $LaMn_3V_4O_{12}$ measured in a magnetic field of 1 T. The crystal structure of an $A$-site-ordered perovskite $AA'_3B_4O_{12}$ is shown in the inset.

by Dudarev *et al* [31]. On the contrary, the V-3$d$ elections are assumed to be itinerant, as described below, and hence were treated simply by GGA without adding $U_{\text{eff}}$. Note that a set of test calculations was also performed with $U_{\text{eff}} = 2$ eV for V-3$d$ electrons as well, but no qualitative difference in the electronic structure (such as band gap opening) was observed. The magnetic energy of $LaMn_3V_4O_{12}$ was also evaluated by effective Heisenberg model calculations.

## III. RESULTS AND DISCUSSION

$LaMn_3V_4O_{12}$ undergoes an AFM transition at $T_N = 44$ K, as shown in Fig. 1, and the paramagnetic Curie constant ($C = 12.75$ emu K/mol) above $T_N$ evidences high-spin $Mn^{2+}$ ($S = 5/2$). The low resistivity ($\sim 20$ m$\Omega$ cm at 300 K) is consistent with the mixed-valence conducting state at the octahedral V site. Thus the 3$d$ electrons of the $A'$-site Mn are localized to give magnetic moments, whereas those of the $B$-site V are itinerant.

The neutron diffraction pattern at 300 K was well reproduced with the $Im\bar{3}$ structure model, consistent with the previous synchrotron x-ray diffraction results, as shown in Fig. 2. The refined structural parameters and selected bond distances and bond angles are summarized in Tables I and II. The bond valence sums [32] of the $A'$-site Mn and the $B$-site V were 2.07 and 3.46, respectively, confirming the $Mn^{2+}$ state and also in good agreement with the previous study [19].

Magnetic reflections were clearly observed in the diffraction pattern obtained at 2 K (below $T_N$), as shown in Fig. 3, demonstrating the existence of a long-range magnetic order. They can be indexed with the magnetic propagation vector $\kappa = [1\,0\,0]$ within the cubic space group $Im\bar{3}$. The allowed irreducible representations (IRs) and their basis vectors (BVs) were determined by magnetic symmetry analysis. Only one IR exists for the Wyckoff site 6$b$, and under the action of $\kappa = [1\,0\,0]$ the three Mn atoms not linked by the $I$ centering become completely independent. Attempts to fit the intensities of the magnetic Bragg reflections using the nine allowed independent parameters diverged, so the number of variables was reduced by constraining the spins to be collinear or to adopt equal

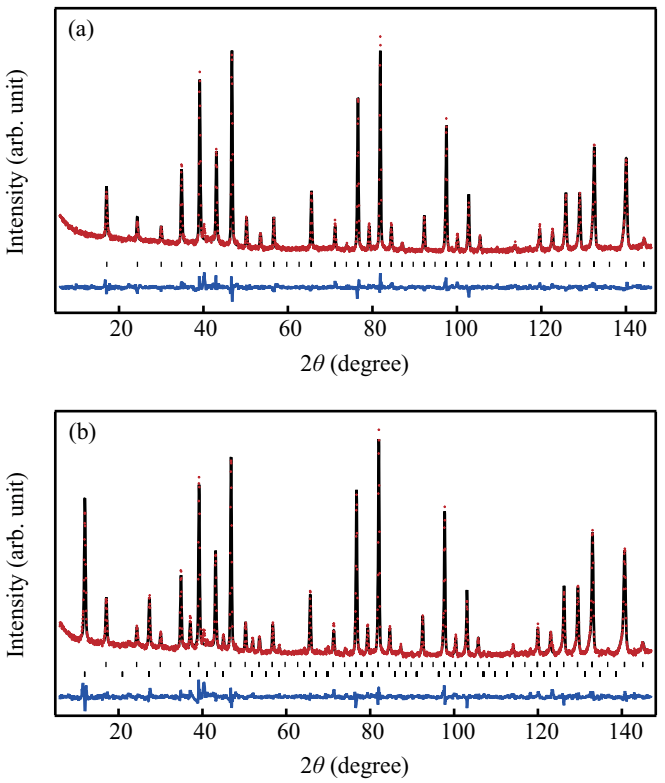


FIG. 2. (Color online) Rietveld plots of the neutron powder diffraction patterns at (a) 300 K and (b) 2 K. The observed (+), calculated (solid line), and difference (bottom) patterns are shown. The ticks indicate the allowed Bragg reflections for nuclear (above) and magnetic (below) phases.

moment values. The best refinement was achieved with a model where the three Mn spins are collinear but adopt strongly differing moment values. This solution gave a moderately good fit to the magnetic intensities ($R_{\text{Mag}} > 8\%$) but is not physically realistic because there are no obvious reasons for the moments to take very different values, and so noncubic magnetic symmetries were explored. Knowing that similar $AA'_3B_4O_{12}$ perovskites can switch between cubic $Im\bar{3}$ and trigonal $R\bar{3}$ structures as a function of doping [33], we repeated the magnetic symmetry analysis assuming space group $R\bar{3}$ with rhombohedral unit cell vectors $\boldsymbol{a}_r = \boldsymbol{b}_c + \boldsymbol{c}_c$, $\boldsymbol{b}_r = \boldsymbol{a}_c - \boldsymbol{b}_c$, $\boldsymbol{c}_r = {}^1\!/_2\,\boldsymbol{a}_c + {}^1\!/_2\,\boldsymbol{b}_c - {}^1\!/_2\,\boldsymbol{c}_c$, where r and c subscripts refer to rhombohedral and cubic cells, and the magnetic peaks are now indexed with $\kappa = [0\,0\,3/2]$. Table III gives the allowed IRs and their BVs for the Wyckoff site 9$e$ where manganese is placed. A very good fit was obtained for the magnetic structure model following BV1 of IR1 ($R_{\text{Mag}} = 5.77\%$). Including the second and/or the third basis vectors of IR1 did not improve the fit. Including the magnetic contributions from $B$-site V ions did not improve the fit either, confirming the nonmagnetic nature of the V ions. In spite of the rhombohedral symmetry of the magnetic structure, neither any peak splitting nor peak broadening expected for a crystallographic rhombohedral distortion were detected. Therefore the cubic $Im\bar{3}$ crystal structure with the rhombohedral $R\bar{3}$ magnetic structure model was used in the final fit to the 2-K data. The 6$b$ Mn site has a large $B_{\text{iso}}$ at both 2 and 300 K, probably due to the

TABLE I. Results of the Rietveld refinement of the neutron powder diffraction data for $LaMn_3V_4O_{12}$ at 2 and 300 K. The Wyckoff positions in space group $Im\bar{3}$, coordinates, isotropic atomic displacement parameter $B_{iso}$, site occupancy, size of the magnetic moment $M_{6b}$ at the 6*b* Mn site, and lattice parameters are listed together with the reliability factors. The refinement of the 2-K data was done including crystal lattice with cubic $Im\bar{3}$ space group and magnetic lattice with rhombohedral $R\bar{3}$ space group, where the latter was constrained to the former with $a_r = b_c + c_c$, $b_r = a_c - b_c$, and $c_r = \frac{1}{2}a_c + \frac{1}{2}b_c - \frac{1}{2}c_c$.

300 K

| Atom | Wyckoff position | *x* | *y* | *z* | $B_{iso}$ (Å$^2$) | Occupancy |
|---|---|---|---|---|---|---|
| La | 2*e* | 0 | 0 | 0 | 0.88(8) | 1 |
| Mn/V | 6*b* | 0 | ½ | ½ | 1.6 (1) | 0.92(1)/0.08(1) |
| V/Mn | 8*c* | ¼ | ¼ | ¼ | 0.3(5) | 0.94(1)/0.06(1) |
| O | 24*g* | 0 | 0.1934(2) | 0.2949(2) | 0.50(2) | 1 |

$a_c = 7.4850(2)$ Å

$R_{wp} = 4.30\%$, $R_B = 4.33\%$, $\chi^2 = 2.38$

2 K

| Atom | Wyckoff position | *x* | *y* | *z* | $B_{iso}$ (Å$^2$) | Occupancy |
|---|---|---|---|---|---|---|
| La | 2*e* | 0 | 0 | 0 | 0.72(8) | 1 |
| Mn/V | 6*b* | 0 | ½ | ½ | 1.38(9) | 0.92/0.08 |
| V/Mn | 8*c* | ¼ | ¼ | ¼ | 1.1(4) | 0.94/0.06 |
| O | 24*g* | 0 | 0.1933(2) | 0.2951(2) | 0.28(2) | 1 |

$M_{6b} = 4.17(4)\,\mu_B$/Mn

$a_c = 7.4679(1)$ Å

$a_r = 10.5612(2)$ Å

$c_r = 6.46737(9)$ Å

$R_{wp} = 5.11\%$, $R_B$(nuclear) $= 4.37\%$, $R_B$(magnetic) $= 5.77\%$, $\chi^2 = 3.32$

coordination geometry by oxygen: it has four long Mn−O bonds on both sides of the $MnO_4$ square plane, forming a strongly anisotropic cage elongated perpendicular to the square plane. The results are summarized in Tables I and II. The refined magnetic moment was 4.17(4) $\mu_B$/Mn, which is consistent with $S = 5/2$ $Mn^{2+}$ at the $A'$ site.

The obtained spin arrangement is illustrated in Fig. 4. All the $Mn^{2+}$ spins lie in kagome layers parallel to the rhombohedral *ab* plane, and the angles between the NN spins (in adjacent kagome layers) and NNN spins (in the same layer) are 60° and 120°, respectively. The magnetic unit cell contains six kagome layers of $Mn^{2+}$ spins with repeat periodicity $2\boldsymbol{c}_r$ perpendicular to the layers. The 60° spin structure in the $A'$-site cubic spin lattice in $LaMn_3V_4O_{12}$ shows a sharp contrast with the FM or G-AFM $A'$-site spin structures reported in other *A*-site-ordered perovskites. In $CaCu_3B_4O_{12}$ with nonmagnetic $Sn^{4+}$ or $Ge^{4+}$ at the *B* site, $Cu^{2+}$ at the $A'$ site makes a cubic spin lattice and the FM-NN interaction between the $Cu^{2+}$ spins gives a parallel spin arrangement. In $CuCu_3Ti_4O_{12}$, on the other hand, AFM third-NN interaction through Cu−O−Ti−O−Cu overcomes the FM-NN interaction and as a result, a collinear G-type antiparallel spin structure is stabilized in the $S = 1/2$ cubic spin lattice [15,16,34]. An *A*-site-ordered perovskite containing $Mn^{3+}$ ions at the $A'$ site, $YMn_3Al_4O_{12}$, shows a similar collinear $A'$-site G-type antiferromagnetism [35].

TABLE II. Selected bond distances and bond angles of $LaMn_3V_4O_{12}$ at 300 and 2 K.

| Temperature | 300 K | 2 K |
|---|---|---|
| Bond distances /Å | | |
| La−O | 2.640(1) | 2.635(2) |
| Mn−O | 2.110(1) | 2.104(1) |
| Mn−O | 2.761(2) | 2.755(1) |
| Mn−O | 3.184(1) | 3.179(2) |
| V−O | 1.9478(4) | 1.9438(4) |
| Bond angles /degree | | |
| V−O−V | 147.8(1) | 147.68(8) |
| V−O−Mn | 105.95(5) | 105.99(9) |

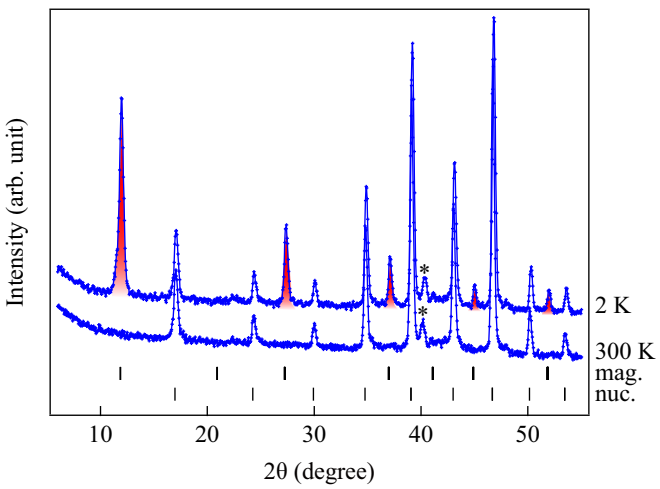


FIG. 3. (Color online) Neutron powder diffraction patterns of $LaMn_3V_4O_{12}$ at 300 and 2 K. The ticks indicate the allowed Bragg reflections for the (lower) cubic nuclear lattice and (upper) rhombohedral magnetic lattice. The magnetic Bragg reflections are shaded red. A single reflection from the vanadium container (*) is observed at around $2\theta = 40°$.

TABLE III. Irreducible representations (IRs) and their basis vectors (BVs) for the Wyckoff site 9*e* in space group $R\bar{3}$ (corresponding to 6*b* Mn site in the cubic nuclear cell) with $\kappa = [0\,0\,3/2]$.

| | IR1 | | | IR2 | | | IR3 | | |
|---|---|---|---|---|---|---|---|---|---|
| | BV1 | BV2 | BV3 | BV1 | BV2 | BV3 | BV1 | BV2 | BV3 |
| $x, y, z$ | 1 0 0 | 0 1 0 | 0 0 1 | 1 0 0 | 0 1 0 | 0 0 1 | 1 0 0 | 0 1 0 | 0 0 1 |
| | 0 0 0 | 0 0 0 | 0 0 0 | 0 0 0 | 0 0 0 | 0 0 0 | 0 0 0 | 0 0 0 | 0 0 0 |
| $-y, x-y, z$ | 0 1 0 | −1 −1 0 | 0 0 1 | 0 −½ 0 | ½ ½ 0 | 0 0 −½ | 0 −½ 0 | ½ ½ 0 | 0 0 −½ |
| | 0 0 0 | 0 0 0 | 0 0 0 | 0 −√3/2 0 | √3/2 √3/2 0 | 0 0 −√3/2 | 0 √3/2 0 | −√3/2 −√3/2 0 | 0 0 √3/2 |
| $-x+y, -x, z$ | −1 −1 0 | 1 0 0 | 0 0 1 | ½ ½ 0 | −½ 0 0 | 0 0 −½ | ½ ½ 0 | −½ 0 0 | 0 0 −½ |
| | 0 0 0 | 0 0 0 | 0 0 0 | −√3/2 −√3/2 0 | √3/2 0 0 | 0 0 √3/2 | √3/2 √3/2 0 | −√3/2 0 0 | 0 0 −√3/2 |

The absence of any detectable rhombohedral cell distortion in $LaMn_3V_4O_{12}$ strongly indicates cubic symmetry, or else the deviation from the cubic model should be negligibly small at most. Thus competing magnetic interactions in the present $LaMn_3V_4O_{12}$ should play an important role in stabilizing the nontrivial 60° spin structure in the cubic spin lattice.

By DFT calculations, total energies were compared between $LaMn_3V_4O_{12}$ with collinear FM and G-AFM arrangements and that with noncollinear 60° AFM arrangement. The results showed that in the $A'$-site cubic spin lattice the experimentally observed noncollinear 60° AFM spin arrangement is 41.6 meV/f.u. (f.u. is formula unit) more stable than the collinear FM arrangement and 30.9 meV/f.u. more stable than the collinear G-AFM arrangement. The result of the electronic structure calculation for $LaMn_3V_4O_{12}$ with the noncollinear 60° spin structure indicates that the Fermi level mainly consists of V-3*d* and O-2*p* bands and that the Mn -3*d* band has a $3d^5$ configuration, as shown in Fig. 5(a). The local magnetic moment at the Mn site is 4.64 $\mu_B$, which agrees well with the value obtained from the neutron diffraction. The results thus confirm that the 3*d* electrons of the divalent Mn ion are localized and contribute to the long-range magnetic ordering, while those of the mixed-valent V ions are itinerant and contribute to the metallic conductivity. The same situation is found in the high-pressure perovskite

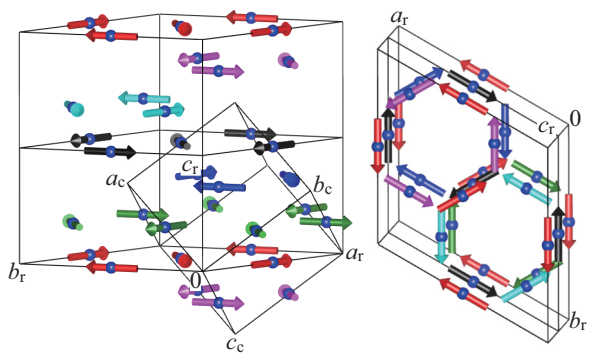


FIG. 4. (Color online) Two views of the spin arrangement of $LaMn_3V_4O_{12}$ at 2 K. The rhombohedral magnetic unit cell is shown in a hexagonal setting, $a_r \times b_r \times 2c_r$. The cubic cell is also drawn in the left figure. The different $z$ heights of the spins are shown by different colors: red ($z = 0$), green ($z = 1/6$), blue ($z = 1/3$), black ($z = 1/2$), sky blue ($z = 2/3$), and purple ($z = 5/6$).

$MnVO_3$, where an incommensurate helimagnetic order of the $Mn^{2+}$ spins is observed [36]. In the obtained band structure of the FM cubic model, there is no nesting vector along the cubic [1 1 1] direction (corresponding to the rhombohedral [0 0 1] direction), which implies that there is no electronic instability that favors rhombohedral distortion.

The origin of the nontrivial spin structure is rationalized here by effective Heisenberg model calculations considering the effect of the NN magnetic interaction ($J_1$), NNN magnetic interaction ($J_2$), and third-NN magnetic interaction ($J_3$) depicted in Fig. 5(b). The details of the calculations are given in the Supplemental Material [37]. If $J_1$ is predominant and $J_2$ and $J_3$ are negligible, the collinear FM spin structure [Fig. 5(c)] is stabilized for $J_1 > 0$ and the collinear G-AFM [Fig. 5(d)] is stabilized for $J_1 < 0$. However, with the contributions of $J_2$ and $J_3$, noncollinear rhombohedral (NR) spin arrangements can be stabilized as shown in the phase diagrams in Fig. 5(g). In the spin structures NR-AFM1 [Fig. 5(e)] and NR-AFM2 [Fig. 5(f)], all the spins lie parallel to the rhombohedral $ab$ plane, and the NN spins in adjacent kagome layers along the $c_r$ axis rotate 60° for NR-AFM1 and 120° for NR-AFM2. Note that the NR spin structures are stabilized for $J_2 < 0$ irrespective of either positive or negative $J_1$. As shown in Fig. 5(g), the experimentally observed NR-AFM1 spin structure is obtained in regions with $J_2 < 0$ and $J_3 < 0$, which suggests that the rhombohedral noncollinear spin structure can be stabilized by competing interactions on a cubic spin lattice without a necessary rhombohedral crystal distortion, although the vector nature of the ordered moments lowers magnetic symmetry to rhombohedral. Hence, the NNN and the third-NN magnetic interactions play crucial roles in giving rise to the nontrivial spin structure of $LaMn_3V_4O_{12}$.

The 60° spin structure of $LaMn_3V_4O_{12}$ appears to be somewhat similar to the spin structure of another $A$-site-ordered perovskite, $CaMn_3Mn_4O_{12}$, where $Mn^{3+}$ spins at the square-planar $A'$ sites and $Mn^{3+}$ and $Mn^{4+}$ spins at the octahedral $B$ sites are helically ordered below 90 K [38–40]. However, the spin arrangement in $CaMn_3Mn_4O_{12}$ stems from the helical orbital order of the localized Mn -3*d* electrons at the $B$ site, in contrast to the case of $LaMn_3V_4O_{12}$, where V-3*d* electrons at the $B$ site are itinerant. We also comment here on the correlation between the magnetism and the electronic transport properties in $LaMn_3V_4O_{12}$. As described above, V-3*d* orbitals strongly hybridize with the O-2*p* orbitals near the Fermi level, giving metallic conduction. However, the negligibly small magnetoresistance of $LaMn_3V_4O_{12}$ [19]

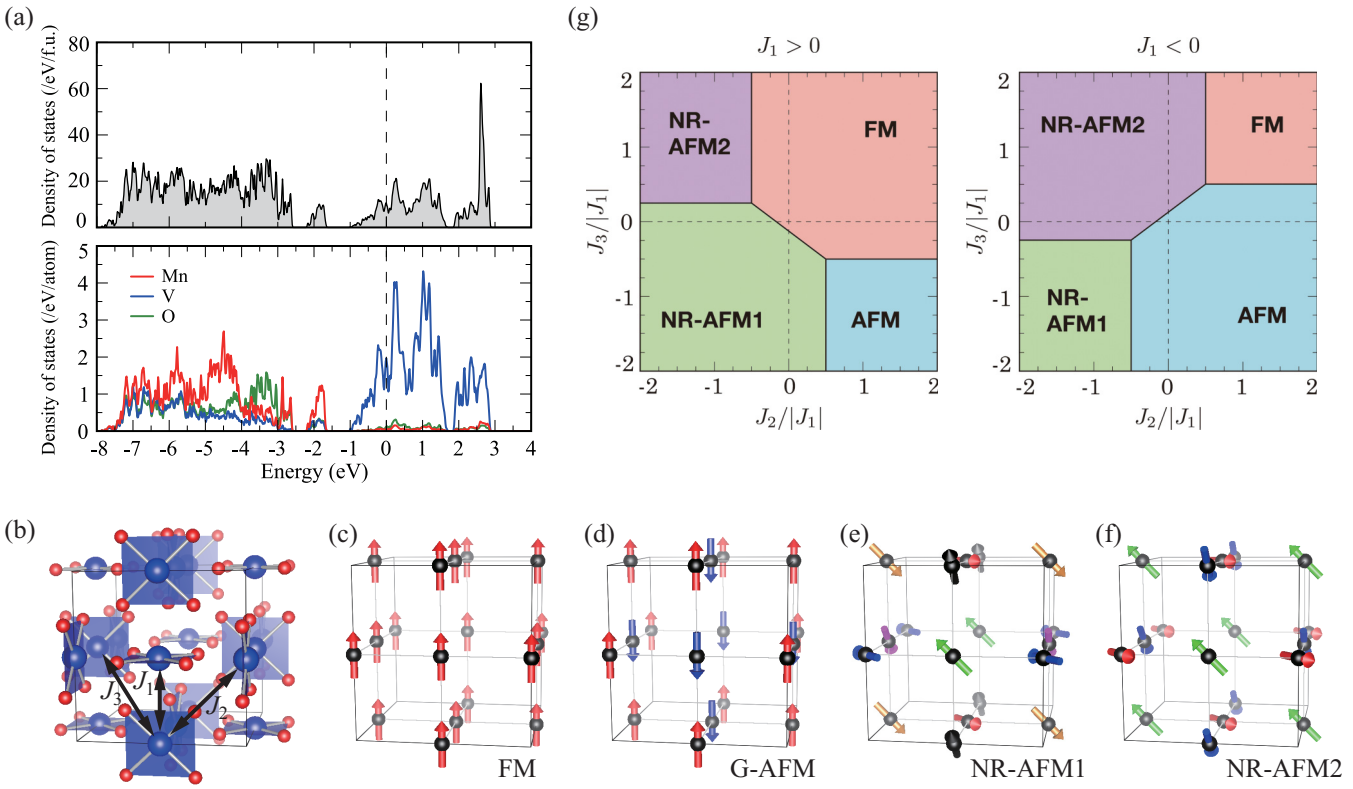


FIG. 5. (Color online) (a) Density of states (DOS) of $LaMn_3V_4O_{12}$. Partial DOS (PDOS) of each constituent atom is also shown in the bottom panel. (b) Mn-Mn spin interactions in $LaMn_3V_4O_{12}$. $J_1$, $J_2$, and $J_3$ are the NN, NNN, and third-NN interactions, respectively. Spin arrangements considered for the magnetic energy calculation: (c) ferromagnetic (FM) arrangement, (d) G-type antiferromagnetic (AFM) arrangement, (e) noncollinear rhombohedral arrangement with the nearest-neighboring spins making an angle of 60° (NR-AFM1), and (f) noncollinear rhombohedral arrangement with nearest-neighboring spins making an angle of 120° (NR-AFM2). (g) Magnetic phase diagrams stabilized by different $J_1$, $J_2$, and $J_3$ magnetic interactions. Cases for $J_1 > 0$ and $J_1 < 0$ are shown.

indicates very weak coupling between the local $Mn^{2+}$ spins at the $A'$ site and itinerant V-3$d$ electrons at the $B$ site. Therefore the itinerant electrons at the $B$-site V do not seem to mediate the magnetic interaction in $LaMn_3V_4O_{12}$.

## IV. CONCLUSIONS

We have found that $A$-site-ordered perovskite $LaMn_3V_4O_{12}$ has a 60° spin structure of high-spin $Mn^{2+}$ moments below $T_N = 44$ K. The electronic structure calculation confirms that the observed noncollinear spin structure is the most stable one. Effective Heisenberg model calculations of the cubic $A'$-site spin lattice revealed that the NNN and third-NN interactions are crucial for stabilizing noncollinear spin structures, and that the competition of the $J_1$, $J_2$, and $J_3$ interactions causes the symmetry breaking of the magnetic system on the cubic lattice to stabilize the 60° spin structure.

## ACKNOWLEDGMENTS

This work was performed under the Strategic Japanese–UK Cooperative Program by the Japan Science and Technology Agency (JST) and the Engineering and Physical Sciences Research Council (EPSRC). The work was partly supported by Grants-in-Aid for Scientific Research (Grants No. 19GS0207 and No. 22740227), by a grant from the Joint Project of Chemical Synthesis Core Research Institutions from the Ministry of Education, Culture, Sports, Science and Technology (MEXT) of Japan, and by the JST-CREST program. Support was also provided by EPSRC, STFC, and the Royal Society, UK.

[1] For a review, see M. L. Plumer, A. Caillé, A. Mailhot, and H. T. Diep, in *Magnetic Systems with Competing Interactions*, edited by H. T. Diep (World Scientific, Singapore, 1994).
[2] H. Kawamura, Can. J. Phys. **79**, 1447 (2001).
[3] R. Kajimoto, H. Mochizuki, H. Yoshizawa, H. Shintani, T. Kimura, and Y. Tokura, J. Phys. Soc. Jpn. **74**, 2430 (2005).
[4] I. Dzyaloshinski, J. Phys. Chem. Solids **4**, 241 (1958).
[5] T. Moriya, Phys. Rev. **120**, 91 (1960).
[6] T. Kimura, S. Ishihara, H. Shintani, T. Arima, K. T. Takahashi, K. Ishizaka, and Y. Tokura, Phys. Rev. B **68**, 060403(R) (2003).
[7] T. Kimura, T. Goto, H. Shintani, K. Ishizuka, T. Arima, and Y. Tokura, Nature (London) **426**, 55 (2003).

[8] G. Lawes, A. B. Harris, T. Kimura, N. Rogado, R. J. Cava, A. Aharony, O. Entin-Wohlman, T. Yildrim, M. Kenzelmann, C. Broholm, and A. P. Ramirez, Phys. Rev. Lett. **95**, 087205 (2005).
[9] I. A. Sergienko and E. Dagotto, Phys. Rev. B **73**, 094434 (2006).
[10] T. Arima, J. Phys. Soc. Jpn. **76**, 073702 (2007).
[11] T. Takeda, Y. Yamaguchi, and H. Watanabe, J. Phys. Soc. Jpn. **33**, 967 (1972).
[12] H. Oda, Y. Yamaguchi, H. Takei, and H. Watanabe, J. Phys. Soc. Jpn. **42**, 101 (1977).
[13] M. Reehuis, C. Ulrich, A. Maljuk, Ch. Niedermayer, B. Ouladdiaf, A. Hoser, T. Hofmann, and B. Keimer, Phys. Rev. B **85**, 184109 (2012).
[14] S. Ishiwata, M. Tokunaga, Y. Kaneko, D. Okuyama, Y. Tokunaga, S. Wakimoto, K. Kakurai, T. Arima, Y. Taguchi, and Y. Tokura, Phys. Rev. B **84**, 054427 (2011).
[15] H. Shiraki, T. Saito, T. Yamada, M. Tsujimoto, M. Azuma, H. Kurata, S. Isoda, M. Takano, and Y. Shimakawa Phys. Rev. B **76**, 140403(R) (2007).
[16] M. Mizumaki, T. Saito, H. Shiraki, and Y. Shimakawa, Inorg. Chem. **48**, 3499 (2009).
[17] Y. Shimakawa, H. Shiraki, and T. Saito, J. Phys. Soc. Jpn. **77**, 113702 (2008).
[18] Y. Shimakawa and T. Saito, Phys. Status Solidi B **249**, 423 (2012).
[19] S. Zhang, T. Saito, M. Mizumaki, W. T. Chen, T. Tohyama, and Y. Shimakawa, J. Am. Chem. Soc. **135**, 6056 (2013).
[20] FULLPROF, D. B. Wiles and R. A. Young, J. Appl. Cryst. **14**, 149 (1981).
[21] J. Rodriguez-Carvajal, BASIREPS: A program for calculating irreducible representations of space groups and basis functions for axial and polar vector properties, Part of the FULLPROF suite of programs available at http://www.ill.eu/sites/fullprof/.
[22] C. Ritter, Solid State Phenom. **170**, 263 (2011).
[23] G. Kresse and J. Hafner, Phys. Rev. B **47**, 558(R) (1993).
[24] G. Kresse and J. Hafner, Phys. Rev. B **49**, 14251 (1994).
[25] G. Kresse and J. Furthmüller, Phys. Rev. B **54**, 11169 (1996).
[26] G. Kresse and J. Furthmüller, Comput. Mater. Sci. **6**, 15 (1996).
[27] J. P. Perdew, K. Burke, and M. Ernzerhof, Phys. Rev. Lett. **77**, 3865 (1996).
[28] J. P. Perdew, M. Ernzerhof, and K. Burke, Phys. Rev. Lett. **78**, 1396 (1997).
[29] P. E. Blöchl, Phys. Rev. B **50**, 17953 (1994).
[30] G. Kresse and D. Joubert, Phys. Rev. B **59**, 1758 (1999).
[31] S. L. Dudarev, G. A. Botton, S. Y. Savrasov, C. J. Humphreys, and A. P. Sutton, Phys. Rev. B **57**, 1505 (1998).
[32] I. D. Brown and D. Altermatt, Acta Crystallogr. Sect. B **41**, 244 (1985).
[33] R. Przenioslo, M. Regulski, I. Sosnowska, and R. Schneider, J. Phys.: Condens. Matter **14**, 1061 (2002).
[34] M. Toyoda, K. Yamauchi, and T. Oguchi, Phys. Rev. B **87**, 224430 (2013).
[35] M. Toyoda *et al.* (unpublished).
[36] M. Markkula, A. M. Arevalo-Lopez, A. Kusmartseva, J. A. Rodgers, C. Ritter, H. Wu, and J. P. Attfield, Phys. Rev. B **84**, 094450 (2011).
[37] See Supplemental Material at http://link.aps.org/supplemental/10.1103/PhysRevB.90.214405 for more details on the effective Heisenberg model calculations.
[38] R. D. Johnson, L. C. Chapon, D. D. Khalyavin, P. Manuel, P. G. Radaelli, and C. Martin, Phys. Rev. Lett. **108**, 067201 (2012).
[39] N. J. Perks, R. D. Johnson, C. Martin, L. C. Chapon, and P. G. Radaelli, Nat. Commun. **3**, 1277 (2012).
[40] G. Zhang, S. Dong, Z. Yan, Y. Guo, Q. Zhang, S. Yunoki, E. Dagotto, and J.-M. Liu, Phys. Rev. B **84**, 174413 (2011).